Electronic Supplementary Information

Ultralow-temperature superelastic polymer aerogel with high strength as great thermal insulators under extreme conditions

Ting Wang, Man-Cheng Long, Hai-Bo Zhao, Bo-Wen Liu, Hai-Gang Shi, Wen-Li An, Shu-Liang Li, Shi-Mei Xu, Yu-Zhong Wang**

Collaborative Innovation Center for Eco-Friendly and Fire-Safety Polymeric Materials (MoE), State Key Laboratory of Polymer Materials Engineering, National Engineering Laboratory of Eco-Friendly Polymeric Materials (Sichuan), College of Chemistry, Sichuan University, Chengdu 610064, China

Correspondence: polymers@vip.126.com (Y.-Z. W.) and haibor7@163.com (H.-B. Z.)

Experimental section

Materials

Chitosan (deacetylation rate: > 80%), melamine, formaldehyde (37 wt % aqueous solution) and acetic acid were supplied by Kelong Chemical Reagent Corp (Chengdu, China). All reagents were of analytical grade and used without further purification. Main Text Paragraph.

Synthesis of cross-linked chitosan aerogels

A 4 wt % aqueous solution of chitosan was prepared by dissolving 4 g of chitosan into 96 g of a 2 vol % aqueous solution of acetic acid. Meanwhile, a melamine-formaldehyde (MF) resin precursor with a solid content of 50% was prepared via dissolving 5 g of melamine and 10 g of formaldehyde solution (37%) at 80 ºC. After that, the MF resin precursor was mixed with chitosan solution at different mass ratios, as shown in table S1. Then the mixed solution was subjected to freeze-casting by controlled unidirectional freezing in a liquid nitrogen bath. The freeze-drying process was conducted by a VFD-1000 lyophilizer (Boyikang Co. Ltd., China) at -20 °C and less than 1 Pa for several days. Finally, the aerogels with stable property were completed by curing at 80 ºC for 24 h in a vacuum oven. The obtained aerogel is named as CmMn aerogel, where C and M represent chitosan and MF, respectively. Furthermore, m and n correspond to the corresponding mass ratios.

Characterization:

The density of aerogels was calculated by the volume and weight of aerogels. The Fourier transform infrared spectroscopy was recorded by a Nicolet FTIR 170SX spectrometer. The morphological microstructures of the samples were characterized by scanning electron micrograph (SEM, Phenom ProX). The compression and resilience properties were characterized by a universal testing machine (CMT4104, SANS Co. Ltd., China), equipped with 10 KN load cells at a strain rate of 10 mm min^{-1}, with a size of 20 mm ×20 mm × 20 mm. The compressive performance at different temperatures

(-60-25 ºC) of the C4M1 was tested by using a dynamic mechanical analyzer (DMA, TA-Q850) at a ramp rate of 5 N/min with a size of 10 mm ×10 mm × 10 mm. The thermal stabilities of aerogels were measured by a TG 209F1 (NETZSCH, Germany) at a heating rate of 10 °C min^{-1} in a N_2 flow of 20 mL min^{-1}. According to ASTM D 2863-2009, the limiting oxygen index (LOI) values were measured by a HC-2C oxygen index meter (Jiangning, China) with a dimension of 10 mm× 10 mm ×100 mm. The combustion behaviors were characterized by a cone calorimeter device (Fire Testing Technology, UK). The specimens were exposed to a heat flux of 50 kW/m^2 with a size of 100 mm ×100 mm × 10 mm. The thermal conductivity was characterized by a heat flow meter apparatus (FOX200, TA, US) using a sample with a size of 100 mm×100 mm×10 mm. The thermal diffusivities of C4M1 in the wide range of temperatures were tested by Laser flash apparatus (LFA, Netzsch LFA 467). Then, the thermal conductivities (k) of the aerogel can be calculated by the following equation.

$$k = \alpha \rho C_p$$

where α is the measured thermal diffusivity, ρ is the density, and Cp is the heat capacity which was determined by the scanning calorimetry (DSC) method. The Cp tested from DSC was 0.886 ± 0.006 J/(g·K).The infrared images of the aerogel were recorded by a FTLR T420 (-40 to 300 °C) infrared thermal camera. The finite element methods (FEM) of bending the cellular walls and honey-comb like aerogel were conducted by the Finite element analysis package Abaqus6.14 and ANSYS 14.5 respectively.

Supplementary analysis

Flame resistance

The flame retardance of CM aerogels was investigated by the limiting oxygen index (LOI) test and cone calorimetry test. As shown in Table S5, the LOI values of the aerogels increased monotonically with the addition of MF resin. The LOI value for C4M1 was as high as 28.5%. The MF resin can both increase the mechanical property and flame retardance.

The cone calorimeter with a heat flux of 50 kW/m^2 was conducted to further investigate the fire-proof capability of the aerogels. The evolution curves of heat release rate are exhibited in Fig. S20, and the corresponding key parameters are listed in Table S6, including time to ignition (TTI), peak of heat release rate (PHRR), total heat release (THR), time to PHRR (TTPHRR), fire growth rate (FIGRA), and residue. The increase of MF resin can significantly decrease the PHRR, especially for the C4M1 aerogel, where the PHRR was only 137.3 kW/m^2, 32 % lower than that of the chitosan aerogel (200.2 kW/m^2). Besides, the CM aerogels manifested a very low FIGRA of 0.2 W/s, exhibiting excellent fire safety. Further, as shown in the Fig. S20b, the CM aerogels manifested the lowest heat release rates in fire among the traditional porous foam materials. More importantly, the C4M1 can withstand even 1200 ºC of butane torch (Fig. S20c) without being ignited. When subjected to the flame, the char firmly integrated on the surface can prevent the flame from spreading and prohibit structural collapse, thus leading to excellent flame retardance. Besides, the MF resin containing plenty of nitrogen is easily decomposed with the formation of the nonflammable gases, such as NH_3, which can dilute the concentration of flammable gases and oxygen in combustion zone.

Thermogravimetric analysis

Fig. S19 shows thermogravimetric analysis (TGA) results of CM aerogels, and the corresponding characteristic thermal degradation datums are summarized in Table S4. The $Td_{5\%}$, which indicates the onset of decomposition, increased with the addition of MF resin ($Td_{5\%}$=127.1-153.3 ºC), in contrast to that of chitosan aerogel ($Td_{5\%}$=117.2 ºC). While, the Td_{max} (the temperature at the maximum weight loss rate) of CM aerogel was about 290 ºC. Therefore, the CM aerogel with low $Td_{5\%}$ loses the elasticity at high temperatures but forms a large amount of thermally stable char, which can effectively resist high-temperature heat.

Forming mechanism of the lamellar thin layer

First, the forming mechanism of the lamellar thin layer was systematically studied by observing the microstructures of aerogels with different MF resin contents (Fig. S2) and densities (Fig. S4). As shown in Fig. S2, with the increase of MF, the primary cell walls were gradually changed from a single layer to two parallel with the formation of macro-channels in the longitudinal section. It was obvious that the double parallel layers of CM aerogels exhibited only at high level MF resin contents (>25 wt%). That is to say, the key to the formation of double parallel layers is the introduction of MF, which can increase the viscosity of the precursor via cross-linking action and bring new phases during freezing. However, according to the SEM images of CM aerogels with same MF resin addition (25 wt%) but different densities (C1M0.25, C1.5M0.375 and C2M0.5), all aerogels manifested that the cell walls consist of two parallel layers (Fig. S4). Therefore, the increase in the viscosity of the precursor is not the main reason. As far as we know, the freeze-drying process usually develops unique pore structures due to the phase separation of the polymer solutions.[1] Polymers exist as single crystals at a very low concentration solution, but exhibit supramolecular architectures of lamellae at a certain concentration.[2] Thus, during the oriented freezing process, the ice crystals grow along supramolecular architectures of polymers, resulting in ordered pore structures after drying. Therefore, the formation of a unique cell wall as shown in Fig. S2 can be explained by the microphase separation of chitosan and melamine formaldehyde resin between the ice fingers.

In order to further study the forming mechanism of the nano pores in the cell walls, the microstructures of C4M1 before post crosslinking were recorded in the Fig. S5. It was found that the cell walls of C4M1 before post crosslinking only consisted of nano-channels (~800 nm) without nano-pores (< 50 nm). Therefore, we can speculate that the nano-channels (~800 nm) were also formed by the microphase separation of chitosan and melamine formaldehyde resin during the freezing process, while the nanopores (< 50 nm) were formed in the post-cross-linking process in which the released of formaldehyde and water during the cross-linking process was conducive to the formation of nanopores (< 50 nm).

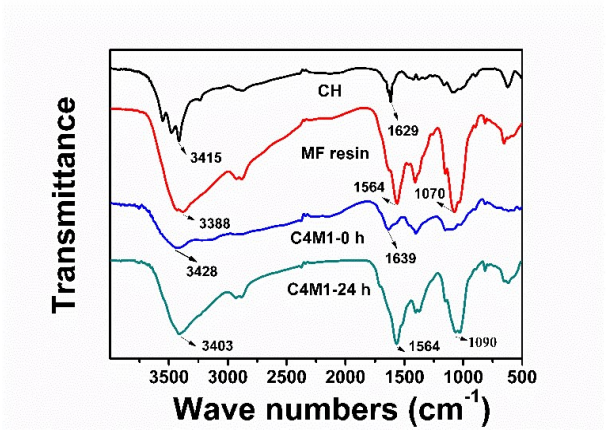

Fig. S1. FTIR spectra of neat CH, MF resin and C4M1 with cross-linking time of 0 h and 24 h.

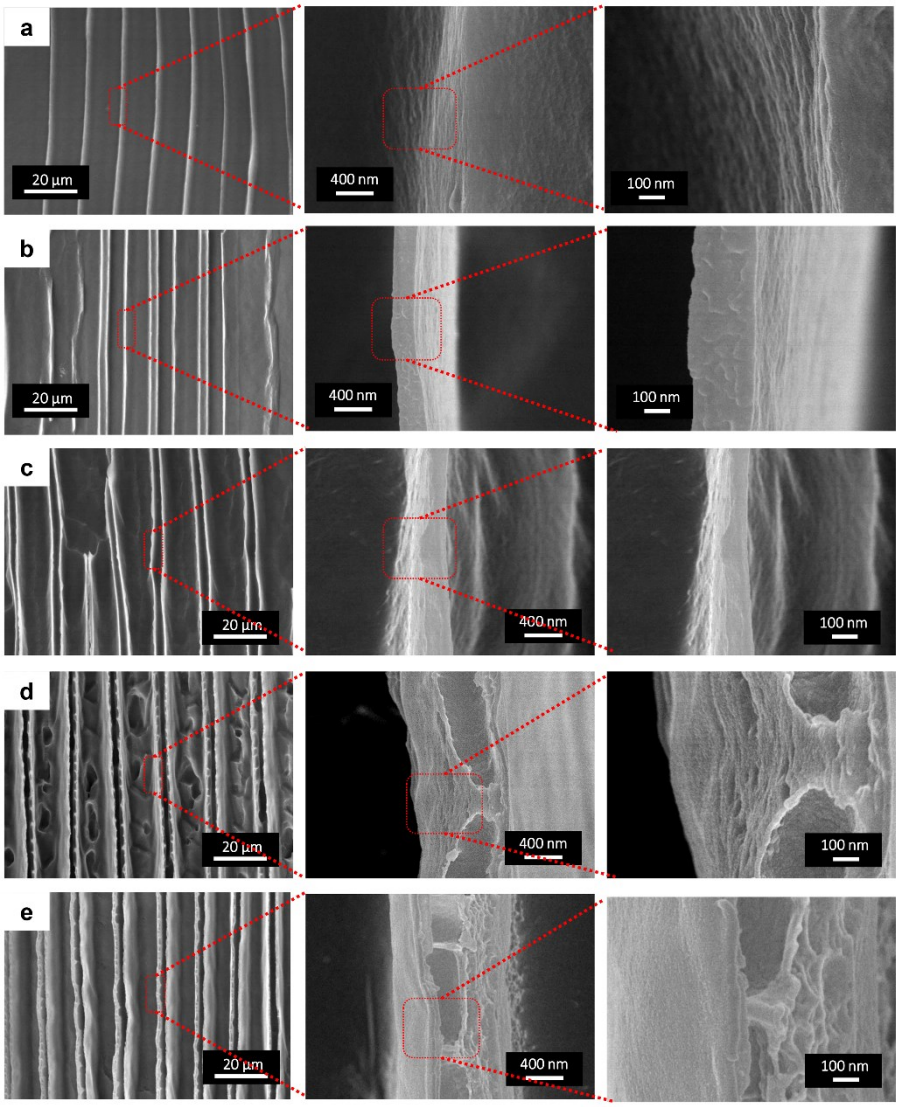

Fig. S2. SEM images for the longitudinal sections of the aerogels: (a) C4, (b) C4M0.1, (c) C4M0.5, (d) C4M1 and (e) C4M2.

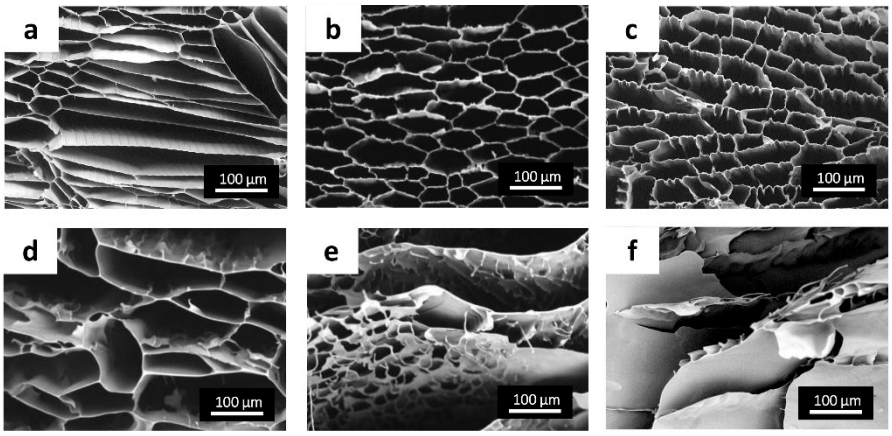

Fig. S3. SEM images for the cross section of the aerogels: (a) C4M0.1, (b) C4M0.5, (c) C4M1, (d) C4F, (e) C4M0.1-I (C4M0.1 with random pores), and (f) C4M1-I (C4M1 with random pores).

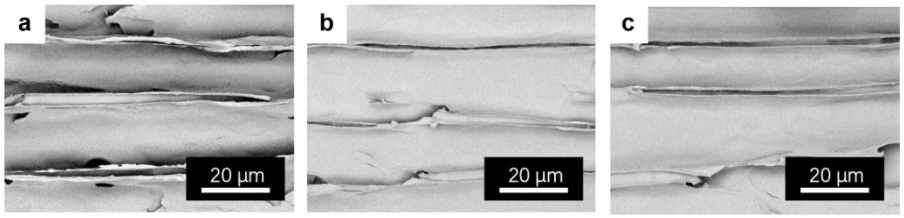

Fig. S4. SEM images for the longitudinal section of the C1M0.25 (a), C1.5M0.375 (b) and C2M0.5 (c).

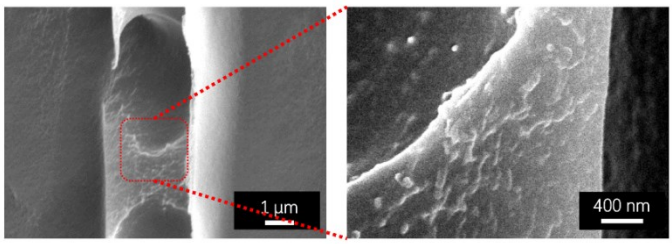

Fig. S5. SEM images for the longitudinal section of the C4M1 aerogel without post-cross-linking treatment.

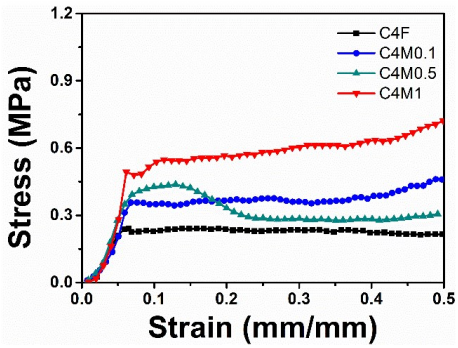

Fig. S6. Compressive stress-strain curves of the aerogels in axial direction.

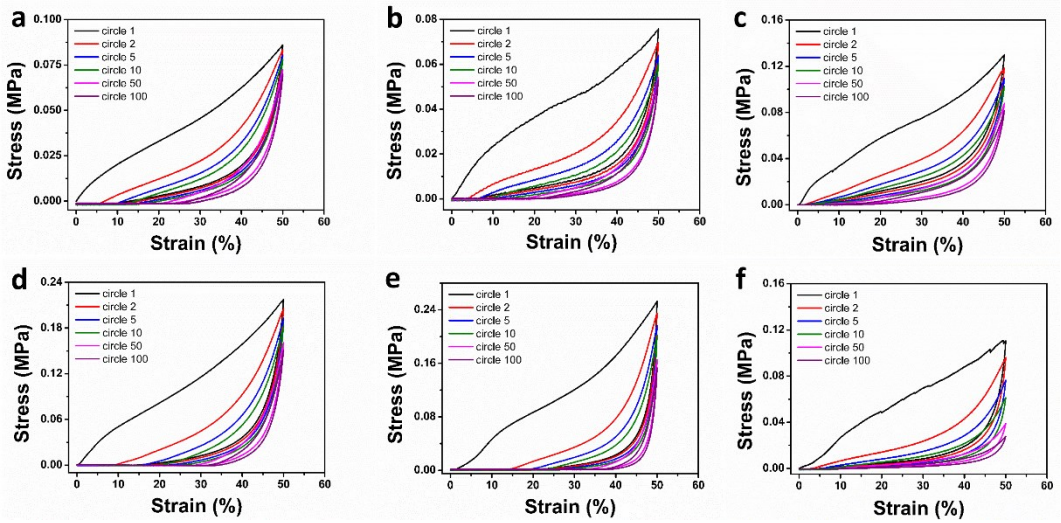

Fig. S7. Stress-strain curves of the aerogels at a maximum strain of 50% for 100 cycles: (a) C4M0.1, (b) C4M0.5, (c) C4M1, (d) C4F, (e) C4M0.1-I (C4M0.1 with random pores), and (f) C4M1-I (C4M1 with random pores).

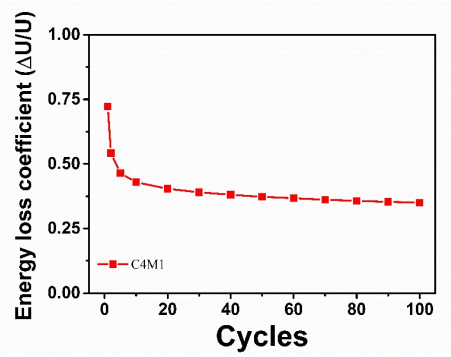

Fig. S8. Energy loss coefficient versus compressive cycles for the C4M1 aerogel.

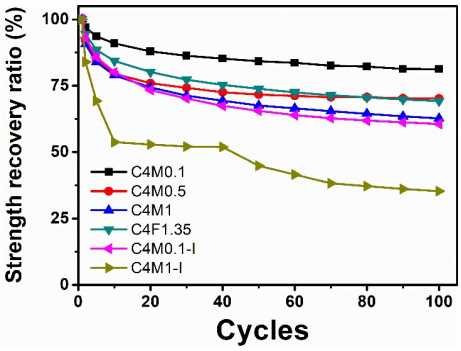

Fig. S9. Strength recovery ratio for the aerogels during 100 compressing/releasing cycles at a constant strain of 50%.

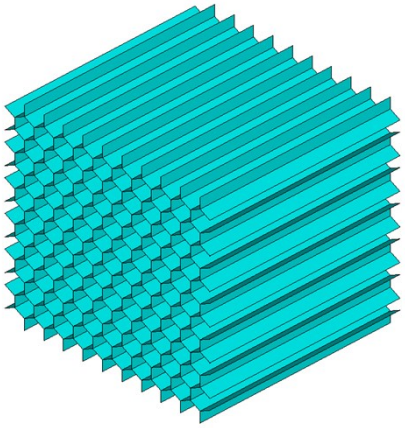

Fig. S10. Honeycomb like structure model for the finite element compression simulations of the C4M1 aerogel.

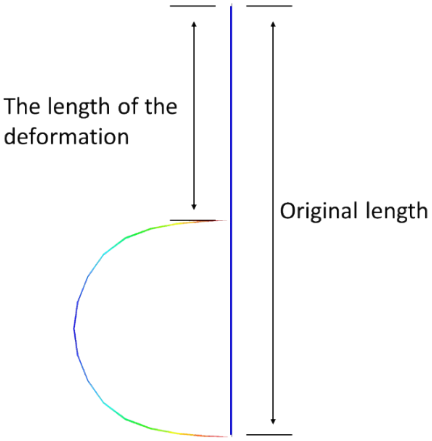

Fig. S11. Schematic illustration of the bending deformation of the cellular walls for the C4M1 aerogel.

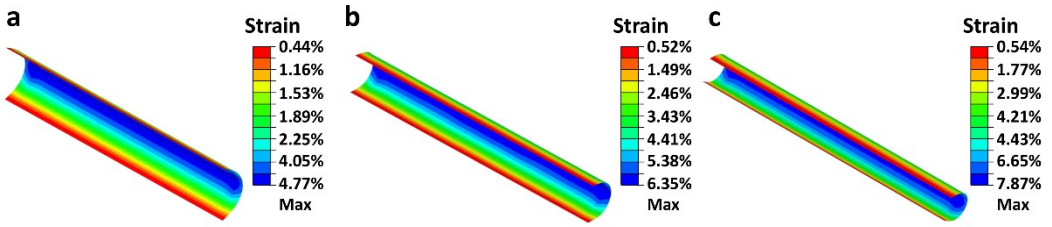

Fig. S12. Finite element simulation of the cellular walls of the C4M1 aerogel with a thickness of 2 μm and length of 80 μm bent with different deformation: (a) 30%, (b) 50% and (c) 70%.

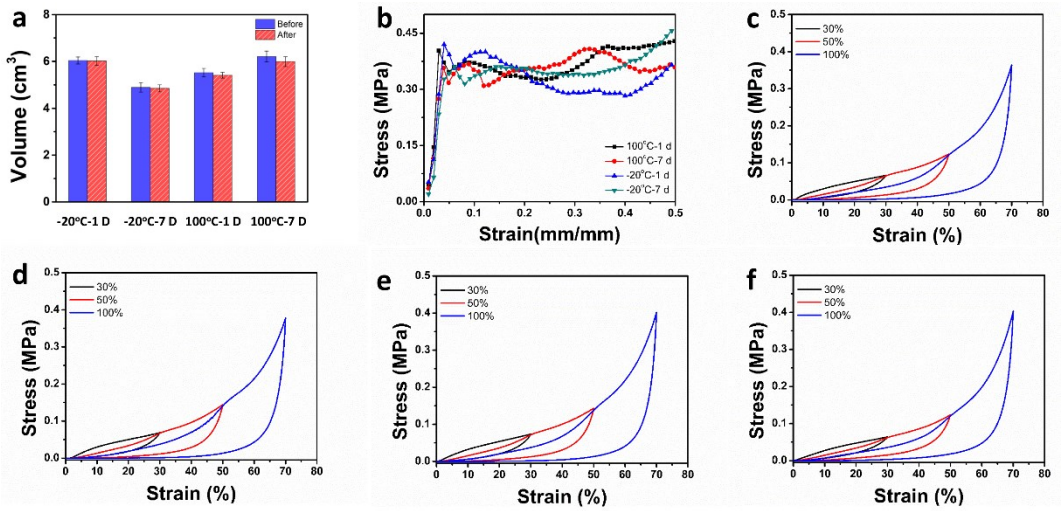

Fig. S13. Dimensional and mechanical stability for the C4M1 aerogels after harsh condition treatments: dimensional stability (a) and compressive stress-strain curves in axial direction (b) after an exposure at -20 ºC or 100 ºC for 1 day or 7 days; cyclic stress-strain curves in radial direction with different maximum strains of 30%, 50%, and 70%, respectively, after an exposure at 100 ºC for 1 d (c) and 7 d (d), and -20 ºC for 1 d (e) and 7 d (f).

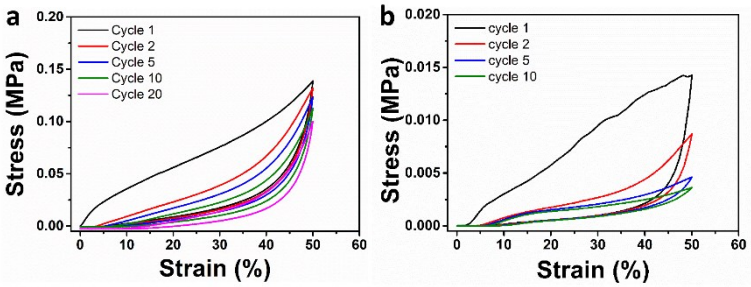

Fig. S14. Stress-strain curves of the C4M1 aerogel (a) and flexible PU foam (b) at a maximum strain of 50% on the surface of dry ice.

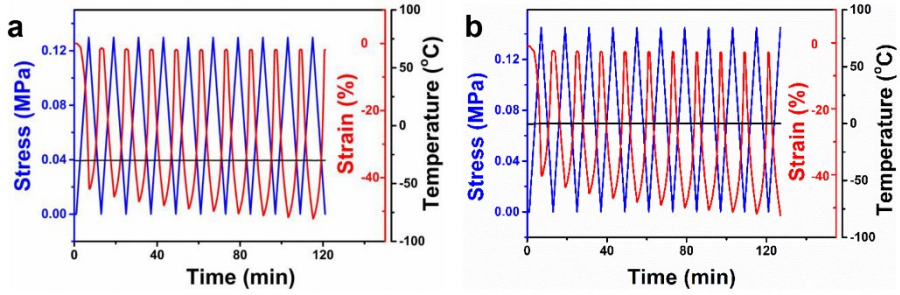

Fig. S15. Stress-strain curves of the C4M1 with a ramping rate of 5 N/min by DMA at -30 ºC (a) and 0 ºC (b).

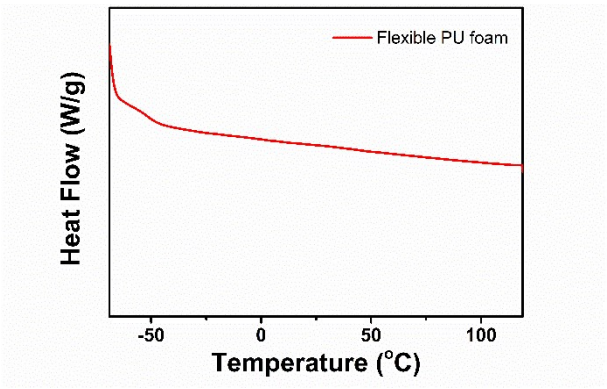

Fig. S16. DSC curve of flexible PU foam.

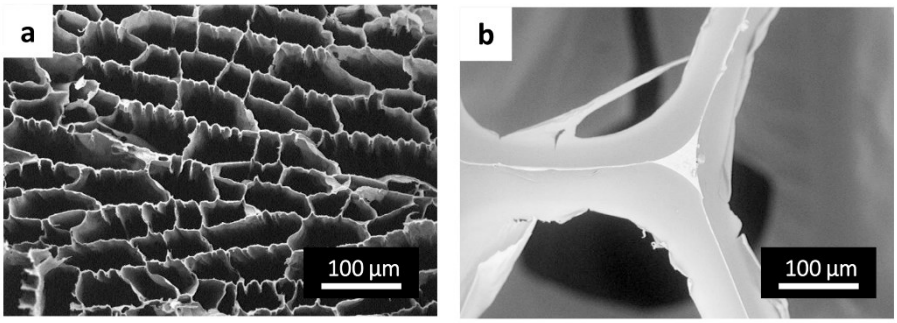

Fig. S17. SEM images for the C4M1 aerogel and flexible PU foam in the same magnification: (a) C4M1 aerogel and (b) flexible PU foam.

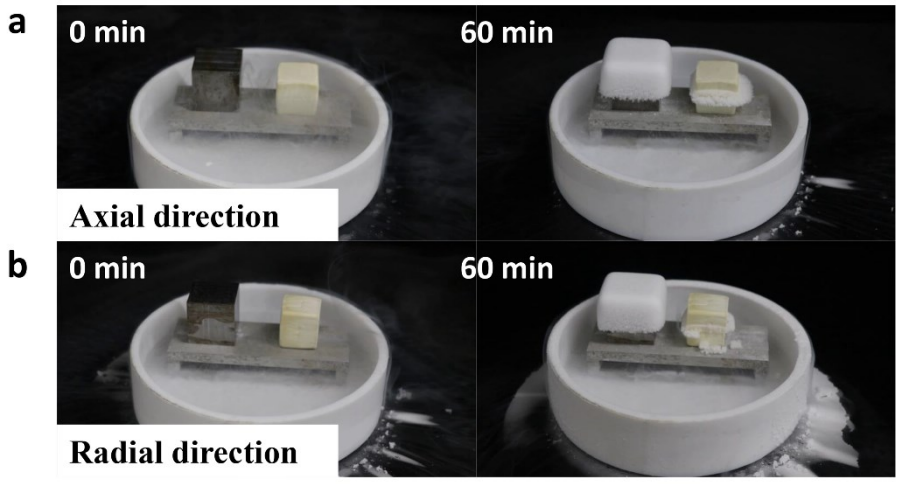

Fig. S18. Optical images for the C4M1 aerogel laid on the surface of the liquid nitrogen for 60 min. During this period, liquid nitrogen was added continuously to maintain the liquid level within a certain range.

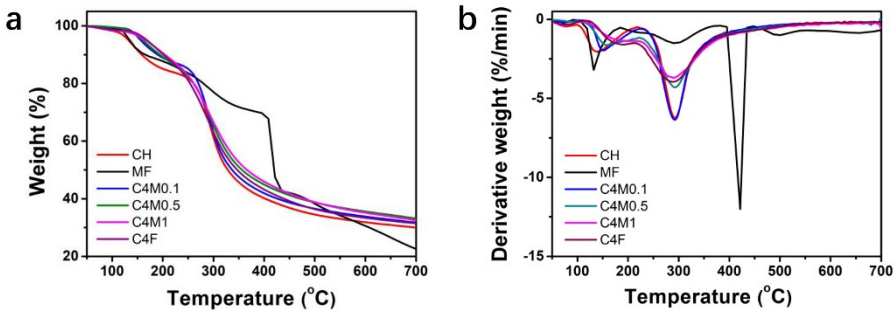

Fig. S19. TGA and corresponding DTG curves of materials in nitrogen: (a) TGA curves and (b) DTG curves.

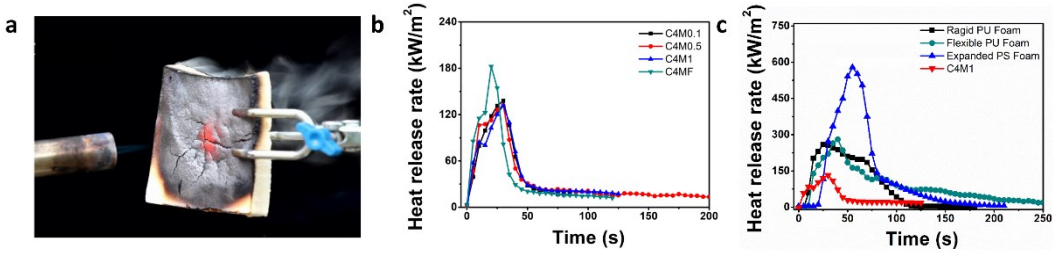

Fig. S20. Fire resistance of materials: (a) image for the C4M1 aerogel being exposed to butane blowtorch flame without ignition; (b) and (c) heat release rate (HRR) curves under a heat radiation of 50kW/m^2.

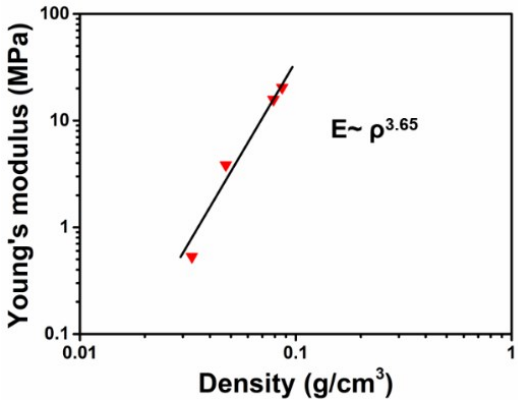

Fig. S21. Relationship between Young's modulus and density of the C4M1 aerogel.

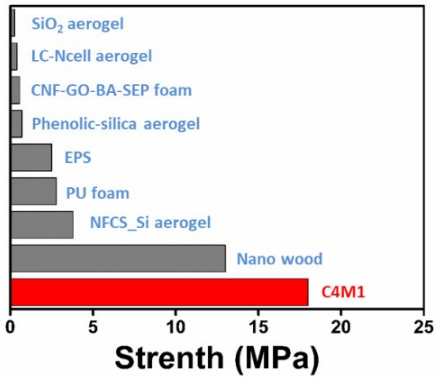

Fig. S22. Comparison of the modulus of C4M1 aerogel in axial direction and other thermal insulation materials.

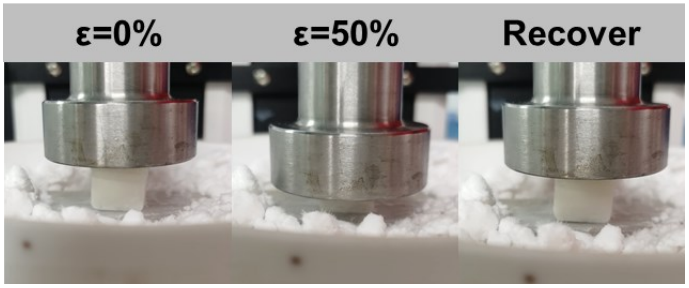

Fig. S23. Optical images for the compressing/releasing process of the C0.5M0.125 aerogel laid on dry ice.

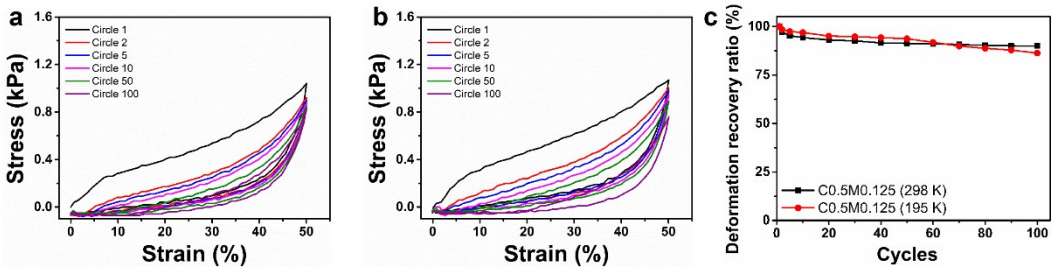

Fig. S24. Stress-strain curves of the C0.5M0.125 at a maximum strain of 50% at room temperature (a) and on the surface of dry ice (b). Deformation recovery ratio of the C0.5M0.125 aerogel at room temperature and on the surface of dry ice during 100 compressing/releasing cycles with a constant strain of 50%.

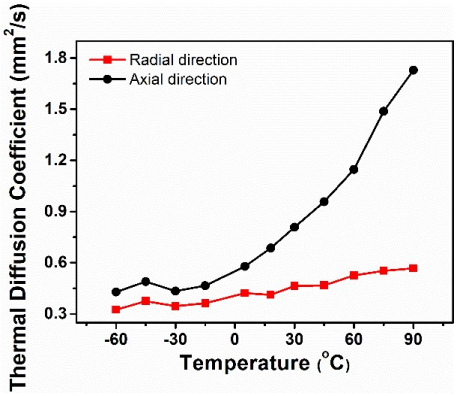

Fig. S25. The thermal diffusion coefficients of C4M1 at different temperatures.

Table S1. The fabrication formulation of aerogels.

Samples	Water (mL)	Chitosan (g)	Melamine (g)	37 wt % Formaldehyde solution (mL)
C4F	100	4.000	-	1.333
C4M0.1	100	4.000	0.067	0.133
C4M0.5	100	4.000	0.333	0.667
C4M1	100	4.000	0.667	1.333
C2M0.5	100	2.000	0.333	0.667
C1.5M0.375	100	1.500	0.250	0.500
C1M0.25	100	1.000	0.166	0.334
C0.5M0.125	100	0.500	0.083	0.167

Table S2. Physical properties of aerogels.

Samples	Density (mg/cm^3)	Modulus (MPa)	Specific modulus (m^2/s^2)
C4F	46.0 ± 0.2	10.22 ± 2.10	222.2±44.9
C4M0.1	53.4 ± 0.2	12.61 ± 1.80	236.1±34.7
C4M0.5	59.5 ± 0.2	14.00 ± 0.60	235.3±11.3
C4M1	64.7 ± 0.2	18.51 ± 1.20	286.1±19.4

Table S3. Physical properties of aerogels after an exposure at -20 ºC or 100 ºC.

Samples	Density (mg/cm^3)	Modulus (MPa)	Specific modulus (m^2/s^2)
C4M1 100 ºC-1 d	63.1 ± 0.2	21.10 ± 2.5	334.3 ± 40.9
C4M1 100 ºC -7 d	66.2 ± 0.2	20.15 ± 3.1	304.4 ± 47.9
C4M1 -20 ºC -1 d	63.6 ± 0.2	17.98 ± 1.8	282.7 ± 29.3
C4M1 -20 ºC -7 d	64.4 ± 0.2	16.37 ± 2.3	254.2 ± 36.6

Table S4. Characteristic TGA Data of aerogels in nitrogen.

Samples	$Td_{5\%}$[a] (°C)	$Tdmax$[b] (°C)	dW/dT[c] (%/min)	Residue (%)
C4M0.1	156.5	292.3	6.36	31.77
C4M0.5	127.1	292.4	4.21	30.24
C4M1	153.3	291.1	3.62	32.19
C4F	168.8	289.0	3.95	31.46
MF	134.3	415	12.05	22.66
CH	117.2	292.2	6.15	29.23

[a] $Td_{5\%}$ is defined as the temperature at which 5 wt% weight loss occurred. [b] Tdmax is defined as the temperature at the maximum weight loss rate. [c] dW/dT is the maximum weight loss rate.

Table S5. The limit oxygen index values (LOI) of aerogels.

Samples	LOI (%)
C4M0.1	27.0±0.5
C4M0.5	28.0±0.5
C4M1	28.5±0.5
C4F	26.0±0.5

Table S6. Characteristic cone calorimetry data of aerogels.

Samples	TTI (s)	PHRR (kW/m^2)	THR (MJ/m^2)	TTPHRR (s)	FIGRA (W/s)	Residue (%)
C4	5	200.2	4.84	22	0.22	1.5
C4M0.1	4	161.0	5.53	26	0.21	3.4
C4M0.5	4	145.3	7.03	30	0.23	4.6
C4M1	5	137.3	5.66	30	0.19	3.5
C4F	3	216.5	4.62	20	0.23	2.8

Table S7. Compressive strength of super-elastic aerogels in the currently published.

Samples	Strength (kPa)
Ceramic nanofibrous aerogel[3]	4.0
BN aerogel[4]	4.5
Nanofibrous aerogel[5]	5.0
Fe7-C5/CNC-C aerogel[6]	8.0
SiC aerogel[7]	10.5
Wood aerogel[8]	11.0
Hard carbon aerogel[9]	11.5
Biomimetic graphene aerogel[10]	17.5
BNNS aerogel[11]	60.0
C4M1 aerogel	130.0

Table S8. Compressive modulus of thermally insulating materials in the currently published.

Samples	Modulus (MPa)
EPS	2.50
PU foam	3.80
Nano wood[12]	13.00
Phenolic-silica aerogel[13]	0.70
LC-N Cell aerogel[14]	0.40
SiO_2 aerogel[15]	0.25
CNF–GO–BA–SEP foam[16]	0.57
NFCS_Si aerogel[17]	2.78
C4M1 aerogel	18.51

Reference

1. Y. Hwang, D.-H. Riu, K.-J. Kim and C.-H. Chang, Mater. Lett., 2014, 131, 174-177.
2. P. V. D. Witte, P. J. Dijkstra, J. W. A. V. D. Berg and J. Feijen, J. Membrane Sci., 1996, 117, 1-31.
3. S. Yang, W. Xueqin, D. Lvye, Y. Jianyong and D. Bin, *Sci. Adv.* , 2018, **4**, 8913-8925.
4. G. Li, M. Zhu, W. Gong, R. Du, A. Eychmüller, T. Li, W. Lv and X. Zhang, *Adv. Funct. Mater.*, 2019, **29**, 1900188.
5. Y. Si, J. Yu, X. Tang, J. Ge and B. Ding, *Nat. Commun.*, 2014, **5**, 5802.
6. Y. Hu, H. Zhuo, Z. Chen, K. Wu, Q. Luo, Q. Liu, S. Jing, C. Liu, L. Zhong, R. Sun and X. Peng, *ACS Appl. Mater. Inter.*, 2018, **10**, 40641-40650.
7. L. Su, H. Wang, M. Niu, X. Fan, M. Ma, Z. Shi and S. W. Guo, *ACS Nano*, 2018, **12**, 3103-3111.
8. J. Song, C. Chen, Z. Yang, Y. Kuang, T. Li, Y. Li, H. Huang, I. Kierzewski, B. Liu, S. He, T. Gao, S. U. Yuruker, A. Gong, B. Yang and L. Hu, *ACS Nano*, 2018, **12**, 140-147.

9. Z. L. Yu, B. Qin, Z. Y. Ma, J. Huang, S. C. Li, H. Y. Zhao, H. Li, Y. B. Zhu, H. A. Wu and S. H. Yu, *Adv. Mater.*, 2019, **31**, e1900651.
10. M. Yang, N. Zhao, Y. Cui, W. Gao, Q. Zhao, C. Gao, H. Bai and T. Xie, *ACS Nano*, 2017, **11**, 6817-6824.
11. X. Zeng, L. Ye, S. Yu, R. Sun, J. Xu and C.-P. Wong, *Chem. Mater.*, 2015, **27**, 5849-5855.
12. T. Li, J. Song, X. Zhao, Z. Yang, G. Pastel, S. Xu, C. Jia, J. Dai, C. Chen, A. Gong, F. Jiang, Y. Yao, T. Fan, B. Yang, L. Wagberg, R. Yang and L. Hu, *Sci. Adv.*, 2018, **4**, eaar3724.
13. Z. L. Yu, N. Yang, V. Apostolopoulou-Kalkavoura, B. Qin, Z. Y. Ma, W. Y. Xing, C. Qiao, L. Bergstrom, M. Antonietti and S. H. Yu, *Angew. Chem. Int. Ed.*, 2018, **57**, 4538-4542.
14. Y. Kobayashi, T. Saito and A. Isogai, *Angew. Chem. Int. Ed*, 2014, **53**, 10394-10397.
15. S. Zhao, Z. Zheng, G. Sèbe, R. Wu, R. V. R. Virtudazo, P. Tingaut and M. M. Koebel, *Adv. Funct. Mater.*, 2015, **25**, 2326-2334.
16. B. Wicklein, A. Kocjan, G. Salazar-Alvarez, F. Carosio, G. Camino, M. Antonietti and L. Bergstrom, *Nat. Nanotechnol.*, 2015, **10**, 277-283.
17. N. Hüsing and U. Schubert, *Angew. Chem. Int. Ed*, 2010, **37**, 22-45.